

Cite this: *Chem. Sci.*, 2024, 15, 6410

All publication charges for this article have been paid for by the Royal Society of Chemistry

# Ultrafast photophysics of an orange–red thermally activated delayed fluorescence emitter: the role of external structural restraint†

Yixuan Gao,<sup>a</sup> Yaxin Wang,<sup>a</sup> Zilong Guo,<sup>ID</sup> \*<sup>a</sup> Yan Wan,<sup>ID</sup> <sup>c</sup> Zheng Xue,<sup>b</sup> Yandong Han,<sup>ID</sup> <sup>b</sup> Wensheng Yang,<sup>ID</sup> <sup>ab</sup> and Xiaonan Ma,<sup>ID</sup> \*<sup>a</sup>

The application of thermally activated delay fluorescence (TADF) emitters in the orange–red regime usually suffers from the fast non-radiative decay of emissive singlet states ( $k_{\text{NR}}^{\text{S}}$ ), leading to low emitting efficiency in corresponding organic light-emitting diode (OLED) devices. Although  $k_{\text{NR}}^{\text{S}}$  has been quantitatively described by energy gap law, how ultrafast molecular motions are associated with the  $k_{\text{NR}}^{\text{S}}$  of TADF emitters remains largely unknown, which limits the development of new strategies for improving the emitting efficiency of corresponding OLED devices. In this work, we employed two commercial TADF emitters (TDBA–Ac and PzTDBA) as a model system and attempted to clarify the relationship between ultrafast excited-state structural relaxation (ES–SR) and  $k_{\text{NR}}^{\text{S}}$ . Spectroscopic and theoretical investigations indicated that  $\text{S}_1/\text{S}_0$  ES–SR is directly associated with promoting vibrational modes, which are considerably involved in electronic–vibrational coupling through the Huang–Rhys factor, while  $k_{\text{NR}}^{\text{S}}$  is largely affected by the reorganization energy of the promoting modes. By restraining  $\text{S}_1/\text{S}_0$  ES–SR in doping films, the  $k_{\text{NR}}^{\text{S}}$  of TADF emitters can be greatly reduced, resulting in high emitting efficiency. Therefore, by establishing the connection among  $\text{S}_1/\text{S}_0$  ES–SR, promoting modes and  $k_{\text{NR}}^{\text{S}}$  of TADF emitters, our work clarified the key role of external structural restraint for achieving high emitting efficiency in TADF-based OLED devices.

Received 19th January 2024  
Accepted 21st March 2024

DOI: 10.1039/d4sc00460d

rsc.li/chemical-science

## Introduction

Organic light-emitting diode (OLED) technology is becoming increasingly attractive due to its great potential for ultra-high definition (UHD) displays.<sup>1–5</sup> As a key factor in the performance of OLED devices, external quantum efficiency ( $\eta_{\text{EQE}}$ ) is described as the ratio between the number of emitted photons and number of injected carriers. In most cases, the  $\eta_{\text{EQE}}$  of OLED devices can be expressed as the product of several contributing terms:<sup>6,7</sup>

$$\eta_{\text{EQE}} = \gamma \times \eta_{\text{EUE}} \times \Phi_{\text{F}} \times \eta_{\text{out}} \quad (1)$$

where the carrier balance factor ( $\gamma$ ) and output coupling factor ( $\eta_{\text{out}}$ ) are associated with the device design and fabrication, respectively, while exciton utilization efficiency ( $\eta_{\text{EUE}}$ ) and fluorescent quantum yield ( $\Phi_{\text{F}}$ ) are regarded as intrinsic properties of the emitters and are associated with corresponding excited-state processes. Spin statistics show that the

recombination of injected electrons and holes leads to 25% singlet and 75% triplet states in OLED emitting layers, respectively,<sup>8,9</sup> while  $\eta_{\text{EUE}}$  gives the fraction of excited states that can decay to the ground state radiatively. Since  $\text{T}_1 \rightarrow \text{S}_0$  decay is spin-forbidden,  $\eta_{\text{EUE}}$  is largely determined by the quantum yield ( $\Phi_{\text{RISC}}$ ) of the reverse intersystem crossing (RISC,  $\text{T}_1 \rightarrow \text{S}_0$ , with rate constant of  $k_{\text{RISC}}$ ), which competes with other  $\text{T}_1$  relaxation routes (radiative  $k_{\text{R}}^{\text{T}}$  and non-radiative  $k_{\text{NR}}^{\text{T}}$ , Fig. S1†):<sup>10,11</sup>

$$\eta_{\text{EUE}} \propto \Phi_{\text{RISC}} = \frac{k_{\text{RISC}}}{k_{\text{RISC}} + k_{\text{R}}^{\text{T}} + k_{\text{NR}}^{\text{T}}} \quad (2)$$

Enormous efforts have been made towards designing thermally activated delayed fluorescence (TADF) emitters with minimized singlet–triplet energy gap ( $\Delta E_{\text{ST}}$ ) and enhanced spin–orbit coupling (SOC) to enable thermal conversion of  $\text{T}_1 \rightarrow \text{S}_1$ , which can potentially push  $\eta_{\text{EUE}}$  to  $\sim 100\%$ .<sup>12–15</sup> Since the  $k_{\text{RISC}}$  of TADF emitters is usually on a time scale of  $10^3$ – $10^5 \text{ s}^{-1}$ ,  $\eta_{\text{EUE}}$  is generally associated with slow dynamics of TADF emitters, which has been intensively investigated.<sup>14,16–18</sup>

In addition to the efficient utilization of current-generated triplet states, the  $\Phi_{\text{F}}$  of TADF emitters greatly affects the  $\eta_{\text{EQE}}$  of the corresponding OLED devices, which describes the ratio of singlet ( $\text{S}_1$ ) states that can be radiatively relaxed to the  $\text{S}_0$  state, *i.e.*, competing plausible relaxation channels for the  $\text{S}_1$  state (Fig. S1†):<sup>19–21</sup>

<sup>a</sup>Institute of Molecular Plus, Tianjin University, Tianjin 300072, P. R. China. E-mail: xiaonanma@tju.edu.cn; zilong.guo@tju.edu.cn

<sup>b</sup>Engineering Research Center for Nanomaterials, Henan University, Kaifeng 475004, P. R. China

<sup>c</sup>College of Chemistry, Beijing Normal University, Beijing 100875, P. R. China

† Electronic supplementary information (ESI) available. See DOI: <https://doi.org/10.1039/d4sc00460d>



$$\Phi_F = \frac{k_R^S}{k_R^S + k_{NR}^S + k_{ISC}} \quad (3)$$

In addition,  $\Phi_F$  includes a contribution from the  $S_1$  state directly generated by injected carriers ( $\Phi_{PF}$ , prompt fluorescence) and converted from the  $T_1$  state ( $\Phi_{DF}$ , delayed fluorescence):

$$\Phi_F = \Phi_{PF} + \Phi_{DF} \quad (4)$$

For organic TADF emitters,  $k_{ISC}$  is usually slow ( $10^7$ – $10^8$  s $^{-1}$ ),<sup>16,22</sup> for which the presence of rapid non-radiative decay is a key factor that can significantly reduce the  $\Phi_F$  of TADF emitters. In a weak coupling regime, the rate constant of the  $S_1$  state non-radiative decay ( $k_{NR}^S$ ) with energy gap ( $\Delta E_{S_1-S_0}$ ) and electronic coupling ( $C$ ) can be described as<sup>23–25</sup>

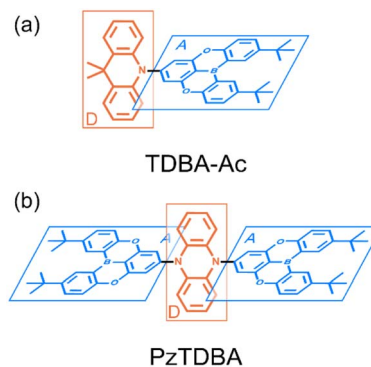
$$k_{NR}^S = \frac{C^2 \sqrt{2\pi}}{\hbar \sqrt{\hbar \omega_M \Delta E_{S_1-S_0}}} \exp \left\{ -\frac{\Delta E_{S_1-S_0}}{\hbar \omega_M} \left[ \ln \left( \frac{\Delta E_{S_1-S_0}}{l \lambda_M} \right) - 1 \right] \right\} \quad (5)$$

where  $\omega_M$  and  $\lambda_M$  represent the frequency and reorganization energy contribution of the promoting vibrational mode, while  $l$  is the number of involved vibrational modes. By assuming  $l = 1$ , eqn (5) can be simplified to the famous energy gap law with the molecule-specific parameter  $\gamma$  as<sup>21,25–27</sup>

$$k_{NR}^S \propto \exp \left( -\frac{\gamma \Delta E_{S_1-S_0}}{\hbar \omega_M} \right) \quad (6)$$

which indicates that  $k_{NR}^S$  increases exponentially with the reduction of the  $S_1 \rightarrow S_0$  energy gap ( $\Delta E_{S_1-S_0}$ ), leading to challenges in the design of long-wavelength TADF emitters with high  $\Phi_F$ .<sup>28–31</sup> As a result, reported TADF emitters in the blue to green regime largely exhibit considerably high  $\Phi_F$ ,<sup>32–34</sup> while the  $\eta_{EQE}$  of the corresponding OLED devices are primarily affected by RISC. In contrast, the small  $\Delta E_{S_1-S_0}$  of orange-red TADF emitters leads to fast  $k_{NR}^S$  competing with the radiative decay of the  $S_1$  state, resulting in a low  $\Phi_F$  and subsequently an unsatisfactory  $\eta_{EQE}$  for OLED devices, although up to 100%  $\eta_{EUE}$  can be expected *via* efficient RISC.<sup>19,28,35–37</sup>

Recently, enormous efforts have been made towards developing long-wavelength TADF-based OLED devices with a high  $\eta_{EQE}$ ,<sup>28,35</sup> in which the low  $\Phi_F$  of TADF emitters is usually regarded as the main obstacle.<sup>28,38–40</sup> Therefore, one can expect opportunities to further improve the  $\eta_{EQE}$  of TADF-based long-wavelength OLED devices by somehow effectively slowing down the  $k_{NR}^S$  rate.<sup>41–44</sup> Recently, Kwon and co-workers reported an acceptor–donor–acceptor (ADA) type TADF emitter (**PzTDBA**, Scheme 1) and realized >30% of the  $\eta_{EQE}$  of orange-red OLED devices.<sup>45</sup> Although the excited-state mechanism that is responsible for the high  $\eta_{EQE}$  is still ambiguous, the reported ~100%  $\Phi_F$  of **PzTDBA** in doping films indicates that non-radiative decay of the  $S_1$  state is nearly terminated, which seems to violate the well-known energy gap law (eqn (6)). Therefore, understanding the underlying ultrafast photophysics that is associated with the slow  $k_{NR}^S$  of **PzTDBA** might provide inspiration for designing high-performance TADF emitters in the long-wavelength regime.



**Scheme 1** Illustrated chemical structure of investigated TADF emitters: (a) **TDBA-Ac**, D–A type; (b) **PzTDBA**, A–D–A type. The charge donors and acceptors are displayed in blue and red, respectively.

In this work, the ultrafast photophysics of an orange-red TADF emitter (**PzTDBA**, ADA-type) and its DA-type analogue (**TDBA-Ac**, deep-blue) was investigated using femtosecond transient absorption (fs-TA), time-resolved fluorescence (tr-FL) and theoretical vibrational analysis.<sup>46</sup> Compared with the one-step D–A twisting of the **TDBA-Ac** emitter, **PzTDBA** exhibits two-step  $S_0/S_1$  excited-state structural relaxation (ES-SR), *i.e.* fast D–A twisting and slow planarization of the Pz group. The promoting vibrational modes associated with the  $S_0/S_1$  ES-SR motions of the **TDBA-Ac** and **PzTDBA** emitters were theoretically identified, which dominate the electronic-vibrational coupling (EVC) of the  $S_1$  state. Meanwhile, promoting modes contribute to fast  $k_{NR}^S$  through the corresponding reorganization energy contribution ( $\lambda_M$ ). In doping films, the  $S_0/S_1$  ES-SR motions of **PzTDBA** are suppressed by external structural restraint, which greatly slows down  $k_{NR}^S$  and leads to ~100%  $\Phi_F$ . Our work established the connection among the  $S_0/S_1$  ES-SR, promoting modes and  $S_1$  state non-radiative decay and indicated the key role of medium rigidity in improving the emitting efficiency of TADF emitters, which should provide inspiration for the future development of TADF emitters.

## Results and discussion

### Low-lying excited states and steady state spectra

Fundamental photophysics of **TDBA-Ac** and **PzTDBA** emitters were first investigated in solvents with different polarities (Table S1†). In OLED devices, TADF emitters are usually doped in a wide-bandgap organic semiconductor as the host. To avoid multi-photon excitation of the host in fs-TA experiments, we prepared doping films (2 wt%) of TADF emitters by employing polystyrene (PS) as the host, and the polarity of the PS medium ( $\epsilon = 2.6$ – $2.7$ ,  $\Delta f = 0.03$ ) was determined to be comparable with toluene (Fig. S2†).<sup>47,48</sup> The UV/Vis absorption and fluorescence spectra of the **TDBA-Ac** and **PzTDBA** emitters in various solutions and films (2 wt%) can be seen in Fig. 1 and S3.† The TD-DFT (M06-2X/6-311G\*\*, PCM = toluene) calculated vertical low-lying singlet and triplet states ( $S_1$ – $S_3$ ,  $T_1$ – $T_3$ ) are listed in Table S2† with the visualized distribution of frontier orbitals (HOMO–2 to LUMO+2) shown in Table S3.† The lowest-lying  $S_1$



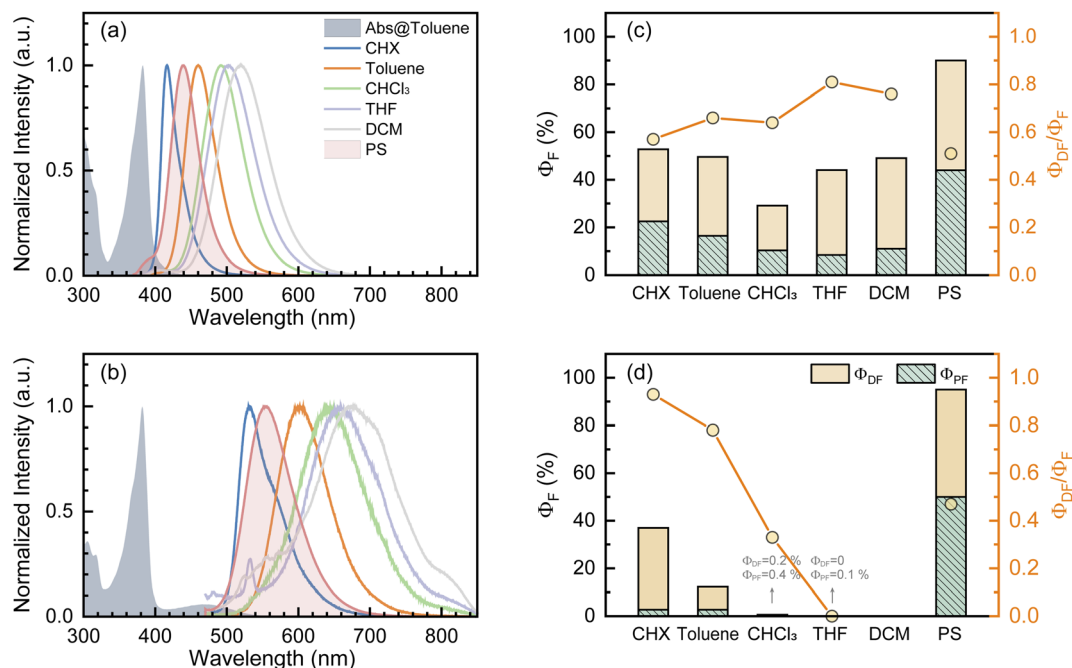


Fig. 1 The steady UV/vis absorption and fluorescence spectra of **TDBA-Ac** (a) and **PzTDDBA** (b) in various solutions and PS doping films. Measured total fluorescence quantum yield ( $\Phi_F$ ), corresponding prompt ( $\Phi_{PF}$ ) and delayed ( $\Phi_{DF}$ ) contribution, as well as the related contribution of the delayed component ( $\Phi_{DF}/\Phi_F$ ) of **TDBA-Ac** (c) and **PzTDDBA** (d).

states of **TDBA-Ac** and **PzTDDBA** are dominated by the  $H \rightarrow L$  transition, corresponding to the charge transfer state (noted as  $^1CT_{DA}$ ) with low oscillator strength, which can be seen as weak absorption of **TDBA-Ac** (400–450 nm) and **PzTDDBA** (420–540 nm). Upon UV excitation, solvatochromism was observed for **TDBA-Ac** and **PzTDDBA**, indicating that the fluorescence emission originated from the lowest-lying  $^1CT_{DA}$  state.<sup>49,50</sup> Intriguingly,  $\sim 1000\text{ cm}^{-1}$  (**TDBA-Ac**) and  $\sim 1400\text{ cm}^{-1}$  (**PzTDDBA**) blue-shifted emissions were observed in PS doping films compared to in toluene (comparable polarity), indicating the presence of multifaceted interactions, which are discussed below.

The  $T_1$  state of **TDBA-Ac** was identified as a local excited state on the acceptor (noted as  $^3LE_A$ ) while the  $T_1$  excitation of **PzTDDBA** was localized on the donor ( $^3LE_D$ ), which allows direct  $T_1 \rightarrow S_1$  RISC ( $^3LE_{D/A} \rightarrow ^1CT_{DA}$ ).<sup>51,52</sup> Meanwhile, the  $T_2$  states of **TDBA-Ac** and **PzTDDBA** were recognized as charge transfer states ( $^3CT_{DA}$ ). With identical orbital wavefunction to the  $^1CT_{DA}$  state, the corresponding  $T_2 \rightarrow S_1$  RISC ( $^3CT_{DA} \rightarrow ^1CT_{DA}$ ) is forbidden.<sup>51,52</sup> By further confirming the CT/LE nature of low-lying singlet/triplet states through natural transition orbital (NTO) analysis (Fig. S4 and S5†) and hole–electron analysis (Table S4†),<sup>53,54</sup> the  $T_1 \rightarrow S_1$  ( $^3LE_{D/A} \rightarrow ^1CT_{DA}$ ) transition was assigned as the accessible RISC channel that is responsible for the delayed fluorescence of **TDBA-Ac** and **PzTDDBA**.

The thermally accessible  $\Delta E_{ST}$  is critical for RISC, while estimating  $\Delta E_{ST}$  through the vertical excitation energy of  $S_1$  and  $T_1$  states was reported to be unreliable.<sup>55</sup> Thus, we further optimized the  $S_1$  and  $T_1$  geometry of the **TDBA-Ac** and **PzTDDBA** emitters to estimate adiabatic  $\Delta E_{ST}^*$ . As listed in Table 1, **TDBA-Ac** and **PzTDDBA** exhibit  $\Delta E_{ST}^*$  of  $\sim 0.3\text{ eV}$  and  $\sim 0.26\text{ eV}$  in low-

polarity media (CHX and TOL,  $\Delta f < 0.02$ ), respectively, facilitating RISC for harvesting  $T_1$  states with moderate  $\langle S_1|\hat{H}_{SO}|T_1\rangle$ . However, increasing to medium polarity (in DCM,  $\Delta f = 0.22$ ) leads to enlarged  $\Delta E_{ST}^*$  ( $>0.33\text{ eV}$ ) for **TDBA-Ac** and **PzTDDBA** with nearly unchanged  $\langle T_1|\hat{H}_{SO}|S_1\rangle$ , which might explain the reduced RISC rate ( $k_{RISC}$ ). Note that the vertical ( $\Delta E_{ST}$ ) and adiabatic ( $\Delta E_{ST}^*$ ) singlet-triplet energy gap does not have a certain magnitude relationship as it depends on multiple factors, such as the different ES-SR in the  $S_1/T_1$  states and steepness of the corresponding potential energy surface (PES), which are simplified as schematic diagrams (Fig. S6†). The total  $\Phi_F$  and corresponding prompt/delayed ( $\Phi_{PF}/\Phi_{DF}$ ) contribution of **TDBA-Ac** and **PzTDDBA** were further measured in different solutions

Table 1 TDDFT calculated vertical ( $E$ ) and adiabatic ( $E^*$ ) excitation energy of the lowest-lying ( $S_1$ ,  $T_1$ ) states and corresponding energy gaps ( $\Delta E_{ST}$ ,  $\Delta E_{ST}^*$ ) of **TDBA-Ac** and **PzTDDBA** in different mediums using PCM as the model; SOC matrix elements for ISC ( $\langle S_1|\hat{H}_{SO}|T_1\rangle$ ) and RISC ( $\langle T_1|\hat{H}_{SO}|S_1\rangle$ ) were calculated by using the linear response approach

	TDBA-Ac			PzTDDBA		
	CHX	TOL	DCM	CHX	TOL	DCM
$E(S_1)/\text{eV}$	3.617	3.626	3.667	3.130	3.142	3.207
$E(T_1)/\text{eV}$	3.250	3.251	3.252	3.015	3.014	3.010
$\Delta E_{ST}/\text{eV}$	0.367	0.375	0.415	0.115	0.128	0.197
$E^*(S_1)/\text{eV}$	3.474	3.482	3.509	2.792	2.804	2.861
$E^*(T_1)/\text{eV}$	3.173	3.173	3.174	2.539	2.538	2.531
$\Delta E_{ST}^*/\text{eV}$	0.301	0.309	0.335	0.253	0.266	0.330
$\langle S_1 \hat{H}_{SO} T_1\rangle/\text{cm}^{-1}$	0.338	0.339	0.294	0.016	0.018	0.058
$\langle T_1 \hat{H}_{SO} S_1\rangle/\text{cm}^{-1}$	0.341	0.341	0.341	0.053	0.052	0.058



and PS doping films. As illustrated in Fig. 1c, **TDBA-Ac** exhibits nearly solvent-independent  $\Phi_F$  (30–50%). With increasing solvent polarity, the solvation of the  $^1\text{CT}_{\text{DA}}$  ( $S_1$ ) state and unchanged energy level of the  $^3\text{LE}_A$  ( $T_1$ ) state resulted in reduced  $\Delta E_{\text{ST}}$ ,<sup>50,56</sup> which is consistent with the observed increasing of the  $\Phi_{\text{DF}}$  contribution ( $\Phi_{\text{DF}}/\Phi_F$ , Fig. 1c). Upon optical excitation,  $S_1 \rightarrow T_1 \rightarrow S_1$  is the only feasible channel for delayed fluorescence,<sup>17,38,57</sup> and increased  $\Phi_{\text{DF}}/\Phi_F$  might correspond to higher  $\Phi_{\text{ISC}}$  and  $\Phi_{\text{RISC}}$ . In contrast, the  $\Phi_F$  of **PzTDBA** rapidly decreased from 37% in non-polar CHX to undetectably low in polar mediums, which implies different relaxation of the photo-generated  $S_1$  state. Intriguingly, **TDBA-Ac** and **PzTDBA** exhibit nearly 100%  $\Phi_F$  and an evenly divided contribution of  $\Phi_{\text{PF}}$  and  $\Phi_{\text{DF}}$  ( $\Phi_{\text{DF}}/\Phi_F \approx 50\%$ ) in PS doping films, indicating that the  $S_1$  state decay is dominantly radiative, while all ISC-generated  $T_1$  states can be harvested through subsequent RISC. Considering the importance of  $\Phi_F$ , resolving the photophysics behind the fully radiative relaxation of orange-red **PzTDBA** in doping film would be of high interest.

### tr-FL and excited-state relaxation

The time-resolved fluorescence (tr-FL) measurements of **TDBA-Ac** and **PzTDBA** were further performed by time-correlated single-photon counting (TCSPC) upon excitation at  $\lambda_{\text{ex}} = 400$  nm.

The resulting traces were fitted as the sum of prompt ( $\tau_{\text{PF}}$ ) and delayed ( $\tau_{\text{DF}}$ ) components (Fig. S7, S8† and Table 2). Combining with measured  $\Phi_{\text{PF}}$  and  $\Phi_{\text{DF}}$ , the rate constants for ISC ( $S_1 \rightarrow T_1$ ,  $k_{\text{ISC}}$ ) and RISC ( $T_1 \rightarrow S_1$ ,  $k_{\text{RISC}}$ ) as well as corresponding  $\Phi_{\text{ISC}}$  and  $\Phi_{\text{RISC}}$  were estimated (Table 2). With calculated SOC matrix elements ( $\langle S_1 | \hat{H}_{\text{SO}} | T_1 \rangle$  and  $\langle T_1 | \hat{H}_{\text{SO}} | S_1 \rangle$ ), we attempted to reproduce the experimentally extracted values of  $k_{\text{ISC}}$  and  $k_{\text{RISC}}$  using the thermal vibration correlation function (TVCF)<sup>16,54,58</sup> and semi-classical Marcus<sup>59,60</sup> approaches. However, as shown in Table S5,† TVCF and Marcus approaches

failed to describe  $k_{\text{ISC}}$  and  $k_{\text{RISC}}$ , which might be attributed to the ignorance of non-Condon effects, such as Herzberg–Teller coupling and spin–vibronic coupling.<sup>61–63</sup> Meanwhile, we noticed that calculation errors for the  $k_{\text{ISC}}$  of **PzTDBA** are much more significant than for **TDBA-Ac**, which might imply higher structural flexibility of **PzTDBA** and will be discussed in detail below. By further estimating the experimental values of  $k_{\text{R}}^{\text{S}}$ ,  $k_{\text{NR}}^{\text{S}}$  and  $k_{\text{NR}}^{\text{T}}$  (Table 2), the quantitative contribution of the plausible relaxation channels was calculated for the  $S_1$  and  $T_1$  states.

As visualized in Fig. 2, the  $S_1$  relaxation of **TDBA-Ac** is dominated by the slightly increased ISC with increased solvent polarity, while the ISC-generated  $T_1$  states can be converted to  $S_1$  with nearly identical  $\Phi_{\text{RISC}}$ , which leads to the nearly unchanged  $\Phi_F$  of **TDBA-Ac** in CHX (0.53), TOL (0.49) and DCM (0.47). In contrast, although ISC still dominates the  $S_1$  decay of **PzTDBA** in CHX and TOL, the generated  $T_1$  states largely decay non-radiatively to  $S_0$  rather than thermally converting to  $S_1$  via RISC, for which a low  $\Phi_F$  was observed in CHX (0.37) and TOL (0.13). In high-polarity DCM, the  $S_1$  decay of **PzTDBA** is predominately occupied by the non-radiative path to  $S_0$ , leading to an undetectable  $\Phi_F$  (<0.01), which might be attributed to the exponentially increased  $k_{\text{NR}}^{\text{S}}$  described by band-gap law with the reducing of the  $S_1 \rightarrow S_0$  energy gap ( $\Delta E_{S_1-S_0}$ ).

Intriguingly, **TDBA-Ac** and **PzTDBA** exhibit nearly identical pattern of  $S_1$  and  $T_1$  decay in PS doping films, which is largely differed with observation in solutions. The  $S_1$  decay of **TDBA-Ac** and **PzTDBA** in PS doping films are dominated by equally divided radiative decay ( $S_1 \rightarrow S_0$ ) and ISC ( $S_1 \rightarrow T_1$ ), while ISC-generated  $T_1$  states can be further converted to  $S_1$  through efficient RISC ( $\Phi_{\text{RISC}} > 0.9$ ). Due to negligible role of non-radiative path in both  $S_1$  (<5%) and  $T_1$  (<10%) state decay, **TDBA-Ac** and **PzTDBA** exhibit unexpectedly high  $\Phi_F$  in PS doping films, which agrees with the reported high  $\eta_{\text{EQE}}$  of corresponding OLED devices.<sup>45,46</sup> However, such high  $\Phi_F$  (0.95) of

Table 2 Measured photophysical data for the **TDBA-Ac** and **PzTDBA** emitters in  $\text{N}_2$ -saturated solutions and PS doping films

	TDBA-Ac				PzTDBA			
	<sup>a</sup> CHX	<sup>a</sup> TOL	<sup>a</sup> DCM	<sup>b</sup> PS	<sup>a</sup> CHX	<sup>a</sup> TOL	<sup>a</sup> DCM	<sup>b</sup> PS
$\tau_{\text{PF}}/\text{ns}$	6.72	21.35	36.15	14.12	8.70	23.95	13.62	38.25
$\tau_{\text{DF}}/\mu\text{s}$	0.15	0.14	0.48	1.21	0.10	0.29	0.23	1.10
$\Phi_F$	0.53	0.49	0.47	0.90	0.37	0.13	<0.01	0.95
$\Phi_{\text{PF}}$	0.23	0.16	0.11	0.44	0.03	0.03	<0.01	0.50
$\Phi_{\text{DF}}$	0.30	0.33	0.36	0.46	0.34	0.10	0	0.45
$^f\Phi_{\text{ISC}}$	0.57	0.67	0.78	0.51	0.93	0.78	0	0.47
$^g\Phi_{\text{RISC}}$	0.39	0.39	0.43	0.82	0.35	0.10	0	0.90
$^c k_{\text{PF}}/10^7 \text{ s}^{-1}$	14.88	4.69	2.77	7.14	11.49	4.17	7.35	2.63
$^d k_{\text{R}}^{\text{S}}/10^6 \text{ s}^{-1}$	33.48	7.70	3.05	31.43	3.10	1.13	—	13.16
$^e k_{\text{NR}}^{\text{S}}/10^6 \text{ s}^{-1}$	30.29	7.82	3.16	3.49	5.28	8.02	73.46	0.69
$^d k_{\text{ISC}}/10^7 \text{ s}^{-1}$	8.50	3.14	2.15	3.65	10.66	3.25	—	1.25
$^c k_{\text{DF}}/10^6 \text{ s}^{-1}$	3.57	3.54	1.01	0.74	3.63	0.43	—	0.86
$^d k_{\text{RISC}}/10^5 \text{ s}^{-1}$	18.75	17.57	4.98	6.69	13.42	0.52	—	8.20
$^d k_{\text{NR}}^{\text{T}}/10^5 \text{ s}^{-1}$	31.50	32.55	9.60	4.49	35.91	4.24	—	4.53

<sup>a</sup> Concentration of  $10^{-5}$  M. <sup>b</sup> Doping concentration of 2 wt%. <sup>c</sup> Calculated by  $k_{\text{PF}} = 1/\tau_{\text{PF}}$  and  $k_{\text{DF}} = 1/\tau_{\text{DF}}$ . <sup>d</sup> Rate constants  $k_{\text{R}}^{\text{S}}$ ,  $k_{\text{ISC}}$ ,  $k_{\text{RISC}}$  and  $k_{\text{NR}}^{\text{T}}$  were calculated using the method described by Adachi *et al.*<sup>10,19</sup> <sup>e</sup> Calculated using  $k_{\text{NR}}^{\text{S}} = k_{\text{PF}} - k_{\text{R}}^{\text{S}} - k_{\text{ISC}}$ . <sup>f</sup> Calculated using  $\Phi_{\text{ISC}} = k_{\text{ISC}}/(k_{\text{ISC}} + k_{\text{R}}^{\text{S}} + k_{\text{NR}}^{\text{S}})$ . <sup>g</sup> Calculated using  $\Phi_{\text{RISC}} = \Phi_{\text{DF}}/(1 - \Phi_{\text{PF}})$ .





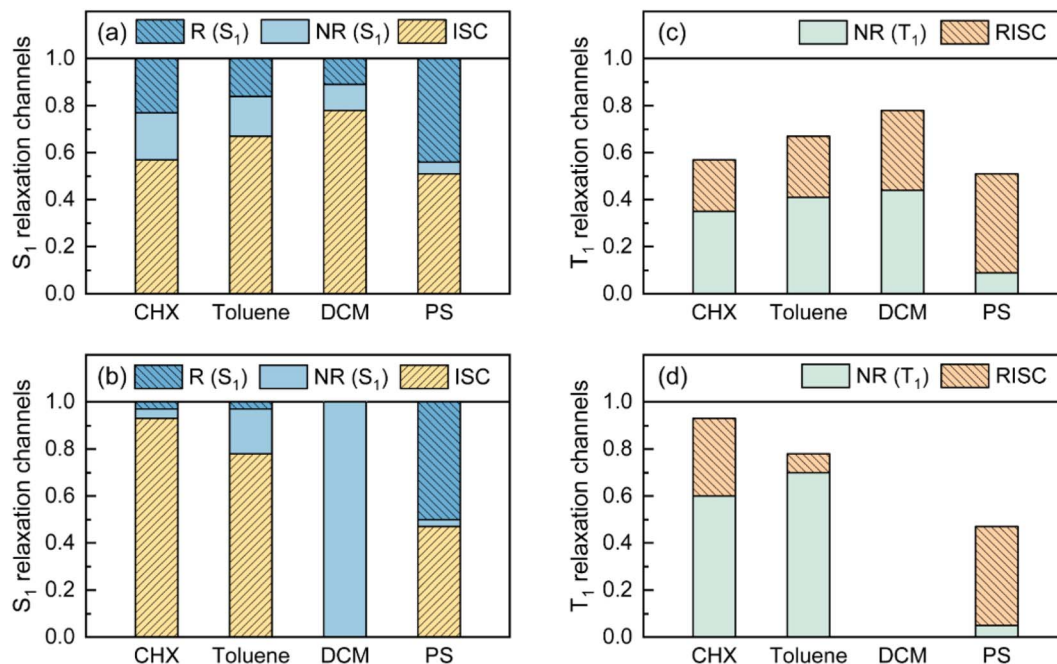


Fig. 2 Visualized contribution of ISC ( $S_1 \rightarrow T_1$ ), radiative (R,  $S_1 \rightarrow S_0$ ) and non-radiative (NR,  $S_1 \rightarrow S_0$ ) decay of  $S_1$  state for TDDBA-Ac (a) and PzTDDBA (b) in various solutions and PS doping films. Contribution of RISC ( $T_1 \rightarrow S_1$ ) and non-radiative (NR,  $T_1 \rightarrow S_0$ ) decay of  $T_1$  state for TDDBA-Ac (c) and PzTDDBA (d) in various solutions and PS doping films, radiative decay of  $T_1$  state was ignored due to low contribution.

PzTDDBA observed in PS doping film seems to be inconsistent with the energy gap law, implying unique photophysics by which non-radiative decay of  $S_1$  state can be greatly suppressed.

### fs-TA and structural relaxation

The fs-TA signal upon UV excitation ( $\lambda_{\text{ex}} = 320$  nm) of TDDBA-Ac and PzTDDBA in CHX solution and PS doping film were recorded by broadband probe ( $\lambda_{\text{probe}} = 350\text{--}750$  nm) with delay times up to 7.0 ns, and the temporal resolution of fs-TA was measured to be  $\sim 90$  fs. As shown in Fig. S9 and S10,<sup>†</sup> the measured fs-TA signals of TDDBA-Ac and PzTDDBA are contributed by negative ground-state bleaching (GSB) in the  $\lambda_{\text{probe}} = 350\text{--}400$  nm regime, and the positive excited-state absorption (ESA) band extended in the longer wavelength region up to  $\lambda_{\text{probe}} = 750$  nm.

Upon UV excitation, high-lying  $S_n$  states can be populated, followed by rapid internal conversion (IC,  $S_n \rightarrow S_1$ ) to the long-lived  $S_1$  state, which explains the dramatically reshaped ESA in the 1 ps delay time.<sup>64,65</sup> For the subsequent delay times of 1 ps to 1 ns, fs-TA evolution visualizes wavepacket motion that highly depends on the topology of  $S_1$  PES.<sup>41,66–68</sup> For instance, the role of the excited-state structural relaxation (ES-SR) in the  $S_1$  state decay of DA- and DAD/ADA-type TADF emitters has been intensively reported.<sup>69–73</sup> Suffering from the poor structural sensitivity of UV/Vis fs-TA,  $S_1/S_0$  ES-SR usually leads to minimized alternation of the ESA shape, which is consistent with the observed fs-TA of TDDBA-Ac and PzTDDBA for 1 ps to 1 ns delay times.<sup>41,74</sup>

For characterizing  $S_1/S_0$  ES-SR, the geometries of TDDBA-Ac and PzTDDBA in the  $S_0$ ,  $S_1$  and  $T_1$  states were optimized using DFT and TD-DFT approaches. The resulting structures are

illustrated in Table S6,<sup>†</sup> while total reorganization energies ( $\lambda_{S_0 \rightarrow S_1}$  and  $\lambda_{S_1 \rightarrow S_0}$ ) were calculated for evaluating the ES-SR of the TDDBA-Ac and PzTDDBA emitters together with the root of the mean squared displacement ( $\text{RMSD}_{S_1/S_0}$ ) between the  $S_0$  and  $S_1$  states (Fig. S11<sup>†</sup>). As listed in Table 3, the calculated values of  $\lambda_{S_0 \rightarrow S_1}$ ,  $\lambda_{S_1 \rightarrow S_0}$  and  $\text{RMSD}_{S_1/S_0}$  indicate a more pronounced ES-ER of PzTDDBA in the  $S_1$  state than TDDBA-Ac, which obviously cannot be attributed to structural extension (DA to ADA structure) as the total reorganization energy and RMSD are not additive. To evaluate the contribution of each of the molecular fragments of the TDDBA-Ac and PzTDDBA emitters to the ES-SR, several critical structural parameters were defined, as illustrated in Fig. S12<sup>†</sup> and measured (Table 3) for the  $S_0$  and  $S_1$  states. Upon vertical excitation, TDDBA-Ac and PzTDDBA initially remain in  $S_0$  geometry in the Franck–Condon (FC) region, following by ES-SR until reaching the global minimum of  $S_1$  PES, *i.e.* optimized  $S_1$  geometry. For TDDBA-Ac,  $S_1/S_0$  ES-SR featured a slight increase in the D–A twisting angle  $\beta$  from  $89.82^\circ$  ( $S_1^{\text{FC}}$ ) to  $92.00^\circ$  ( $S_1^{\text{T}}$ ), while the dihedral angles of the Ac ( $\alpha$ ) and TDDBA ( $\gamma$ ) framework bending remained nearly unchanged in the  $S_1$  state decay. In contrast, ADA-type PzTDDBA exhibits higher flexibility than that of TDDBA-Ac. In addition to the fast motion of the D–A twisting angle ( $\beta$ ) from  $79.72^\circ/79.06^\circ$  ( $S_1^{\text{FC}}$ ) to  $89.02^\circ/91.43^\circ$  ( $S_1^{\text{T}}$ ), framework planarization of the center donor (Pz) was observed as the dihedral angle ( $\alpha$ ) increased from  $164.57^\circ$  ( $S_1^{\text{T}}$ ) to  $180.00^\circ$  ( $S_1^{\text{TP}}$ ). The simultaneous  $S_0$ – $S_1$  state changing of  $\alpha$  and  $\beta$  angles may correspond to a two-step  $S_1/S_0$  ES-SR ( $S_1^{\text{FC}} \rightarrow S_1^{\text{T}} \rightarrow S_1^{\text{TP}}$ ), which has been widely reported,<sup>75,76</sup> *i.e.* fast D–A twisting ( $S_1^{\text{FC}} \rightarrow S_1^{\text{T}}$ ) followed by slow framework planarization ( $S_1^{\text{T}} \rightarrow S_1^{\text{TP}}$ ). Target analysis was further performed to acquire



**Table 3** DFT and TD-DFT (M06-2X, 6-311G\*\*, PCM = toluene) calculated optimal geometric parameters of TDBA-Ac and PzTDBA in the  $S_0$ ,  $S_1$  and  $T_1$  states, as well as the calculated total reorganization energy and RMSD associated with the  $S_1$  state ES-SR<sup>a</sup>

	TDBA-Ac			PzTDBA		
	* $\alpha$ (°)	** $\beta$ (°)	*** $\gamma$ (°)	* $\alpha$ (°)	** $\beta_{1/\beta_2}$ (°)	*** $\gamma_{1/\gamma_2}$ (°)
$S_0$ geometry	176.50	89.82	11.36	164.57	79.72/79.06	11.56/10.99
$S_1$ geometry	175.45	92.00	12.12	180.00	89.02/91.43	11.65/11.37
$T_1$ geometry	176.57	90.82	4.77	180.00	88.60/91.33	11.40/11.40
$\lambda_{S_0 \rightarrow S_1}$ (cm <sup>-1</sup> )	1161			2790		
$\lambda_{S_1 \rightarrow S_0}$ (cm <sup>-1</sup> )	1273			2552		
RMSD $_{S_1/S_0}$ (Å)	0.053			0.241		

<sup>a</sup> \*Bending dihedral angle of donor (Ac/Pz); \*\*donor-acceptor twisting angle; \*\*\*bending dihedral angle of acceptor (TDBA).

quantitative information on  $S_1/S_0$  ES-SR that may play a key role in the  $S_1$  state relaxation. By including three or four sequential decay processes, measured fs-TA data can be well-reproduced by the displayed decay-associated spectra (DAS) of each decay components and concentration evolution of each transient species (Fig. 3), while species-associated spectra (SAS) can be seen in Fig. S13 and S14.<sup>†</sup>

The initial decay (A  $\rightarrow$  B) with 300–400 fs time constant was accompanied by considerable ESA reshaping, corresponding to rapid IC ( $S_n \rightarrow S_1$ ). The fs-TA was subsequently dominated by  $S_1/S_0$  ES-SR until the wavepacket reached the global minimum of  $S_1$  PES. For **PzTDBA**, highlighted two-step  $S_1/S_0$  ES-SR (B  $\rightarrow$  C  $\rightarrow$  D, *i.e.*  $S_1^{FC} \rightarrow S_1^T \rightarrow S_1^{TP}$ ) predicted by calculated  $S_0$  and  $S_1$  geometries was observed, featuring a slight ESA reshaping. The

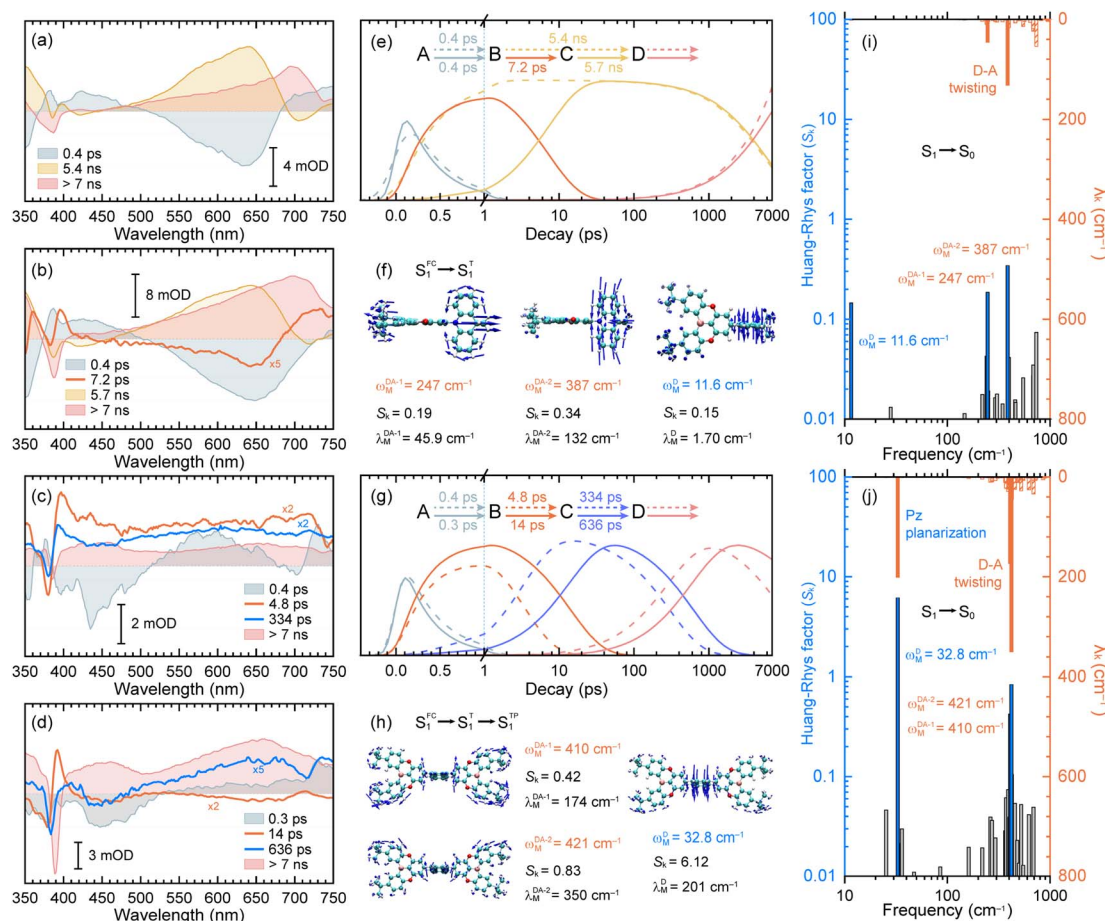


**Fig. 3** The decay-associated spectra (DAS) extracted from the fs-TA data of TDBA-Ac in CHX solution (a) and PS doping film (b) as well as PzTDBA in CHX solution (c) and PS doping film (d). Fitted concentration evolution of TDBA-Ac (e) and PzTDBA (g) in CHX solution (dashed lines) and PS doping film (solid lines). Promoting vibrational modes of TDBA-Ac (f) and PzTDBA (h) with large contribution to the HR factors. Calculated HR factors and reorganization energy contribution of each vibrational mode of TDBA-Ac (i) and PzTDBA (j) for the  $S_1 \rightarrow S_0$  transition in CHX solution. The dominant modes displayed in (f) and (h) are highlighted correspondingly.

observed fast (4.8 ps in CHX,  $S_1^{\text{FC}} \rightarrow S_1^{\text{T}}$ ) and slow (334 ps in CHX,  $S_1^{\text{T}} \rightarrow S_1^{\text{TP}}$ ) steps correspond to D–A twisting ( $\beta_1/\beta_2$  angles) and Pz planarization ( $\alpha$  angle), respectively.

For **TDBA-Ac**, one-step  $S_1/S_0$  ES-SR was observed (7.2 ps,  $S_1^{\text{FC}} \rightarrow S_1^{\text{T}}$ ) in the PS doping film, corresponding to the D–A twisting ( $\beta$  angle), which is comparable with the fast  $S_1/S_0$  ES-SR step of **PzTDBA**. However,  $S_1/S_0$  ES-SR of **TDBA-Ac** was unobservable in CHX, which might be attributed to a less pronounced  $S_0 \rightarrow S_1$  structural change than for **PzTDBA**, *i.e.* nearly unchanged  $\beta$  angle in the  $S_0$  (89.82°) and  $S_1$  (92.00°) states.

Intriguingly, the extracted time constants of D–A twisting ( $S_1^{\text{FC}} \rightarrow S_1^{\text{T}}$ , 14.0 ps) and Pz planarization ( $S_1^{\text{T}} \rightarrow S_1^{\text{TP}}$ , 636 ps) of **PzTDBA** in the PS doping film are 2–3 times slower than corresponding  $S_1/S_0$  ES-SR steps in CHX (Fig. 3g and S15†), implying a higher potential barrier for  $S_1$  PES, which is consistent with our fs-TA observations for multiple-resonance emitters.<sup>77</sup> Moreover, slow  $S_1$  isomerization of azo-benzene embedded in polymer films was reported previously, attributing to external structural restraint from polymer micro-networks.<sup>78</sup>

As discussed above, the fluorescence emission of **PzTDBA** was strongly quenched ( $\Phi_{\text{F}} = 0.37$  in CHX) in solutions due to the presence of fast non-radiative decay, while a high  $\Phi_{\text{F}}$  (>0.95) in the PS doping film may be feasible if non-radiative  $S_1 \rightarrow S_0$  decay can be greatly suppressed. Our fs-TA data revealed higher  $S_1/S_0$  ES-SR barriers of **PzTDBA** in PS doping films than in CHX, which might imply the presence of an underlying association between  $S_1/S_0$  ES-SR and the non-radiative decay of the  $S_1$  state, *i.e.* restrained  $S_1/S_0$  ES-SR leads to suppressed non-radiative decay. Conversely,  $k_{\text{NR}}^{\text{S}}$  was described to be highly correlated with promoting vibrational modes by the energy gap law (eqn (5)).<sup>21,23</sup> Thus, we attempted to unveil the underlying relationship among the  $S_1/S_0$  ES-SR, promoting modes and non-radiative decay of the  $S_1$  state.

### Vibrational analysis and non-radiative decay

The energy gap law (eqn (5)) clearly describes how promoting vibrational modes affect  $k_{\text{NR}}^{\text{S}}$  through their vibrational frequency ( $\omega_{\text{M}}$ ) and reorganization energy ( $\lambda_{\text{M}}$ ), while promoting modes are vibrational modes that are considerably involved in the EVC of the  $S_1$  state through a pronounced Huang-Rhys (HR) factor ( $S_{\text{k}}$ ).<sup>24,79,80</sup> We further calculated the  $S_{\text{k}}$  and  $\lambda_{\text{k}}$  contribution of each of the vibrational modes involved in the  $S_1 \rightarrow S_0$  transition (Fig. 3i and j), in which the promoting modes associated with the  $k_{\text{NR}}^{\text{S}}$  of **TDBA-Ac** and **PzTDBA** are illustrated in Fig. 3f and h, respectively.

As shown in Fig. 3j and h, three promoting modes were identified for the  $S_1 \rightarrow S_0$  transition of **PzTDBA** due to considerable  $S_{\text{k}}$ . The modes at 410  $\text{cm}^{-1}$  ( $\omega_{\text{M}}^{\text{DA-1}}$ ) and 421  $\text{cm}^{-1}$  ( $\omega_{\text{M}}^{\text{DA-2}}$ ) correspond to symmetric and asymmetric D–A twisting and exhibit considerable reorganization energy contributions ( $\lambda_{\text{M}}^{\text{DA-1}} = 174 \text{ cm}^{-1}$  and  $\lambda_{\text{M}}^{\text{DA-2}} = 350 \text{ cm}^{-1}$ ), which are associated with the fast  $S_1/S_0$  ES-SR step observed on fs-TA of **PzTDBA**, *i.e.*  $S_1^{\text{FC}} \rightarrow S_1^{\text{T}}$  with the D–A twisting motion. For **TDBA-Ac** (Fig. 3i and f), the corresponding  $S_1/S_0$  ES-SR of D–A twisting is associated with

promoting modes at  $\omega_{\text{M}}^{\text{DA-1}} = 247 \text{ cm}^{-1}$  and  $\omega_{\text{M}}^{\text{DA-2}} = 387 \text{ cm}^{-1}$  with substantially lower  $\lambda_{\text{M}}^{\text{DA-1}}$  (45.9  $\text{cm}^{-1}$ ) and  $\lambda_{\text{M}}^{\text{DA-2}}$  (132  $\text{cm}^{-1}$ ), which is consistent with its rigid structure predicted theoretically, *i.e.* less pronounced  $S_1/S_0$  ES-SR than **PzTDBA**.

Meanwhile,  $S_1 \rightarrow S_0$  decay of **PzTDBA** features a promoting mode at  $\omega_{\text{M}}^{\text{D}} = 32.8 \text{ cm}^{-1}$  with a surprisingly high HR factor ( $S_{\text{k}} = 6.12$ ) and considerable reorganization energy ( $\lambda_{\text{M}}^{\text{D}} = 201.1 \text{ cm}^{-1}$ ), corresponding to the bending motion of the Pz framework, which is clearly associated with the observed slow  $S_1/S_0$  ES-SR step of **PzTDBA**, *i.e.*  $S_1^{\text{T}} \rightarrow S_1^{\text{TP}}$ . Intriguingly, this particular mode was also observed for **TDBA-Ac** at  $\omega_{\text{M}}^{\text{D}} = 11.6 \text{ cm}^{-1}$  with a much lower HR factor ( $S_{\text{k}} = 0.15$ ) and a two orders of magnitude lower reorganization energy contribution ( $\lambda_{\text{M}}^{\text{D}} = 1.70 \text{ cm}^{-1}$ ) than that of **PzTDBA**, indicating that it was excluded from the  $S_1 \rightarrow S_0$  decay of **TDBA-Ac**. As a result, the second  $S_1/S_0$  ES-SR step ( $S_1^{\text{T}} \rightarrow S_1^{\text{TP}}$ ) was absent from the fs-TA signal of **TDBA-Ac**.

Furthermore, we investigated the influence of medium polarity on the promoting modes of the **TDBA-Ac** and **PzTDBA** emitters. As shown in Fig. S16,† for **PzTDBA** in DCM solution, an extra promoting mode at 15.4  $\text{cm}^{-1}$  was observed with considerable  $S_{\text{k}}$  but ignorable  $\lambda_{\text{k}}$ , which might be less associated with the non-radiative decay of  $S_1$  state **PzTDBA**. In contrast, a promoting mode at 12.4  $\text{cm}^{-1}$  was observed for **TDBA-Ac** with considerable  $S_{\text{k}}$  (8.71) and  $\lambda_{\text{k}}$  (108.23  $\text{cm}^{-1}$ ) in DCM solution, which is very different from the case of **TDBA-Ac** in low-polarity solvents, indicating that the  $S_1/S_0$  ES-SR of **TDBA-Ac** (DA-type) is more evidentially coupled with charge transfer than **PzTDBA** (ADA-type).

As discussed above, the one- (**TDBA-Ac**,  $S_1^{\text{FC}} \rightarrow S_1^{\text{T}}$ ) and two-step (**PzTDBA**,  $S_1^{\text{T}} \rightarrow S_1^{\text{TP}}$ )  $S_1/S_0$  ES-SR are directly associated with promoting vibrational modes that are considerably involved in the EVC of the  $S_1$  state through their HR factor. Meanwhile, promoting modes contribute to the  $k_{\text{NR}}^{\text{S}}$  of the  $S_1$  state through corresponding  $\lambda_{\text{M}}$ , which implies that  $S_1/S_0$  ES-SR can significantly affect  $k_{\text{NR}}^{\text{S}}$  (and subsequently  $\Phi_{\text{F}}$ ) through the promoting vibrational modes (Fig. 4). For instance, the one-step  $S_1/S_0$  ES-SR of **TDBA-Ac** is associated with vibrational modes with low  $S_{\text{k}}$  and  $\lambda_{\text{M}}$ , while the promoting modes associated with the two-step  $S_1/S_0$  ES-SR of **PzTDBA** have much higher  $S_{\text{k}}$  and  $\lambda_{\text{M}}$ . As a result, the non-radiative channel plays a minor role in the  $S_1$  decay of structurally rigid **TDBA-Ac**, while the emission of structurally flexible **PzTDBA** is severely hampered by the fast non-radiative decay of the  $S_1$  state. Furthermore, the two-step  $S_1/S_0$  ES-SR motions of **PzTDBA** are greatly suppressed in the PS doping films due to the external structural restraint, for which the  $S_1$  non-radiative decay associated with the promoting modes might be correspondingly weakened, leading to the greatly improved  $\Phi_{\text{F}}$  of **PzTDBA** in the doping films. In this sense, the external structural restraint for  $S_1/S_0$  ES-SR motions might be critical for achieving a high  $\eta_{\text{EQE}}$  for TADF-based OLED devices.

To directly verify the influence of the external structural restraint on the  $S_1$  non-radiative decay of **PzTDBA**, we measured temperature-dependent emission spectra of **PzTDBA** in polyethylene oxide (PEO) doping films (Fig. S18†). With a glass transition temperature ( $T_{\text{g}}$ ) of 220 K, PEO provides a “softer”





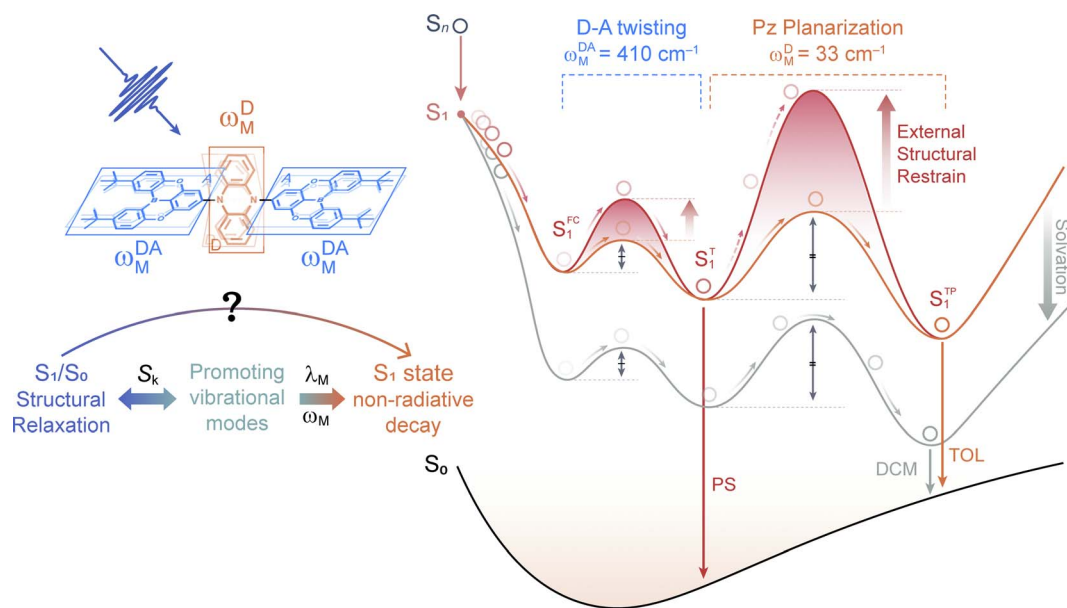


Fig. 4 Simplified energetic diagram illustrating two-step ES-SR ( $S_1^{FC} \rightarrow S_1^T$  and  $S_1^T \rightarrow S_1^{TP}$ ) of **PzTDBA** in low-polarity solution (orange line, TOL), high-polarity solution (cyan line, DCM) and PS doping film (red line). The double arrows represent the potential barriers of D–A twisting ( $S_1^{FC} \rightarrow S_1^T$ ) and Pz planarization ( $S_1^T \rightarrow S_1^{TP}$ ).

microenvironment than PS ( $T_g = 373$  K) and can be further “softened” by increasing the temperature.<sup>81,82</sup> As a TADF emitter, **PzTDBA** was expected to be more fluorescent at higher temperatures due to faster RISC. However, we observed clear fluorescence quenching with increasing temperature in the 297–347 K range, indicating that non-radiative decay was enhanced in the medium with reduced external structural restraint, which is consistent with our analysis described above.

Note that we cannot perform vibrational analysis for TADF emitters with the presence of the external structural restraint, but we speculate that the  $\lambda_M$  of the promoting modes of **PzTDBA** might be greatly reduced due to the external structural restraint, in agreement with slowed  $S_1/S_0$  ES-SR motions in the doping films, especially the Pz bending mode ( $\omega_M^D$ ) associated with the slow  $S_1/S_0$  ES-SR step ( $S_1^T \rightarrow S_1^{TP}$ ) might be terminated. As a result,  $S_1^T$  instead of  $S_1^{TP}$  might dominate the emission of **PzTDBA** in the PS doping films (see Fig. 4), which explains the observed blue-shifted emission in the PS doping film compared with the case in toluene solution, which has comparable polarity to the PS medium. Meanwhile, the emission of **PzTDBA** in solutions mainly originates from  $S_1^{TP}$  due to the accessible barrier of  $S_1^T \rightarrow S_1^{TP}$ , which thus suffers from the plague of non-radiative decay (Fig. 4).

Last but not least, in addition to the  $S_1$  state, we noticed that **TDBA-Ac** and **PzTDBA** exhibit a suppressed non-radiative decay channel of the  $T_1$  state in the PS doping films compared to in solutions (Fig. 2c and d), which inspired us to consider the role of  $T_1/S_0$  ES-SR in the non-radiative decay of the  $T_1$  state. As shown in Fig. S17,<sup>†</sup> **TDBA-Ac** exhibits several vibrational modes with considerable  $S_k$  in the region  $<100$   $\text{cm}^{-1}$ , but the low  $\lambda_M$  implies that ES-SR may not be strongly associated with non-radiative  $T_1 \rightarrow S_0$  decay. In contrast, the promoting modes of

**PzTDBA** at  $32.9$   $\text{cm}^{-1}$  and  $421/410$   $\text{cm}^{-1}$  contribute considerable  $\lambda_M$ , while pronounced  $T_1/S_0$  ES-SR was indicated (Table 3), including Pz bending and D–A twisting. Therefore, it might be plausible that the non-radiative  $T_1 \rightarrow S_0$  decay is similarly associated with two  $T_1/S_0$  ES-SR motions, because the non-radiative  $T_1 \rightarrow S_0$  decay of **PzTDBA** was strongly suppressed in the PS doping film due to the external structural restraint. However, unlike  $S_1$  relaxation, without direct spectroscopic evidence of  $T_1/S_0$  ES-SR in different media, verifying this hypothesis requires further investigation.

## Conclusions

To summarize, we performed a comprehensive investigation of the photophysics of two TADF emitters, **TDBA-Ac** (DA-type, blue light) and **PzTDBA** (ADA-type, orange-red light), using fs-TA, tr-FL and theoretical approaches. Compared with the one-step  $S_1/S_0$  ES-SR ( $S_1^{FC} \rightarrow S_1^T$ ) of **TDBA-Ac**, the  $S_1$  state decay of **PzTDBA** is dominated by two steps,  $S_1/S_0$  ES-SR ( $S_1^{FC} \rightarrow S_1^T \rightarrow S_1^{TP}$ ), while greatly slowed  $S_1/S_0$  ES-SR motions of **PzTDBA** were observed in the PS doping films due to the external structural restraints. Vibrational analysis indicated that the  $S_1/S_0$  ES-SR motions are directly associated with the promoting modes that are considerably involved in the EVC of the  $S_1$  state through their own  $S_k$ , while the promoting modes contribute to fast  $k_{NR}^S$  via  $\lambda_M$ . In doping films, the external structural restraint leads to suppressed  $S_1/S_0$  ES-SR and reorganization energy contribution of the promoting modes, resulting in slowed  $k_{NR}^S$  and a highly fluorescent  $S_1$  state that is favorable for OLED application. With **TDBA-Ac** and **PzTDBA** as model systems, we established the connection among the  $S_0/S_1$  ES-SR, promoting modes and  $k_{NR}^S$  of TADF emitters, which indicated the key role of the external





structural restraint in obtaining high  $\Phi_F$  TADF emitters. Our work also provides a new direction for OLED design, and it might be necessary to take the rigidity of host materials used for the emitting layer into consideration to avoid emission quenching through fast non-radiative decay associated with the  $S_1/S_0$  ES-SR of TADF emitters, especially for TADF emitters with a relatively small band gap, which might be a useful reference for future OLED application.

## Data availability

All experimental and calculational data are available from the corresponding author upon reasonable request.

## Author contributions

Yixuan Gao: conceptualization, methodology, investigation, data curation, formal analysis, visualization, and writing – original draft; Yaxin Wang: methodology, data curation, formal analysis, and validation; Zilong Guo: investigation, visualization, project administration, and supervision; Yan Wan: methodology and resources; Zheng Xue and Yandong Han: resources and project administration; Wensheng Yang: supervision, resources, and funding acquisition; Xiaonan Ma: conceptualization, formal analysis, funding acquisition, supervision, and writing – review and editing.

## Conflicts of interest

The authors declare no competing financial interest.

## Acknowledgements

We acknowledge the financial support from the National Key Research & Development Program of China (Grant No. 2020YFA0714603 and 2020YFA0714604). We thank Dr Yingli Niu (Beijing Jiaotong University) for his useful tutoring on MOMAP calculation and Dr Lei Zhou (HORIBA Scientific, Beijing) for valuable discussion on tr-FL measurements.

## Notes and references

- 1 Y.-Z. Shi, H. Wu, K. Wang, J. Yu, X.-M. Ou and X.-H. Zhang, *Chem. Sci.*, 2022, **13**, 3625–3651.
- 2 Y. Huang, E.-L. Hsiang, M.-Y. Deng and S.-T. Wu, *Light: Sci. Appl.*, 2020, **9**, 105.
- 3 Z. Yang, Z. Mao, Z. Xie, Y. Zhang, S. Liu, J. Zhao, J. Xu, Z. Chi and M. P. Aldred, *Chem. Soc. Rev.*, 2017, **46**, 915–1016.
- 4 G. Hong, X. Gan, C. Leonhardt, Z. Zhang, J. Seibert, J. M. Busch and S. Bräse, *Adv. Mater.*, 2021, **33**, 2005630.
- 5 H.-W. Chen, J.-H. Lee, B.-Y. Lin, S. Chen and S.-T. Wu, *Light: Sci. Appl.*, 2017, **7**, 17168.
- 6 M. A. Baldo, D. F. O'Brien, Y. You, A. Shoustikov, S. Sibley, M. E. Thompson and S. R. Forrest, *Nature*, 1998, **395**, 151–154.
- 7 K. Goushi, K. Yoshida, K. Sato and C. Adachi, *Nat. Photonics*, 2012, **6**, 253–258.
- 8 L. J. Rothberg and A. J. Lovinger, *J. Mater. Res.*, 1996, **11**, 3174–3187.
- 9 M. Pope, H. P. Kallmann and P. Magnante, *J. Chem. Phys.*, 1963, **38**, 2042–2043.
- 10 Q. Zhang, B. Li, S. Huang, H. Nomura, H. Tanaka and C. Adachi, *Nat. Photonics*, 2014, **8**, 326–332.
- 11 H. Noda, H. Nakanotani and C. Adachi, *Sci. Adv.*, 2018, **4**, eaao6910.
- 12 H. Uoyama, K. Goushi, K. Shizu, H. Nomura and C. Adachi, *Nature*, 2012, **492**, 234–238.
- 13 J. M. Kaminski, A. Rodríguez-Serrano, F. Dinkelbach, H. Miranda-Salinas, A. P. Monkman and C. M. Marian, *Chem. Sci.*, 2022, **13**, 7057–7066.
- 14 H. Noda, X.-K. Chen, H. Nakanotani, T. Hosokai, M. Miyajima, N. Notsuka, Y. Kashima, J.-L. Brédas and C. Adachi, *Nat. Mater.*, 2019, **18**, 1084–1090.
- 15 M. Cai, M. Auffray, D. Zhang, Y. Zhang, R. Nagata, Z. Lin, X. Tang, C.-Y. Chan, Y.-T. Lee, T. Huang, X. Song, Y. Tsuchiya, C. Adachi and L. Duan, *Chem. Eng. J.*, 2021, **420**, 127591.
- 16 Q. Peng, D. Fan, R. Duan, Y. Yi, Y. Niu, D. Wang and Z. Shuai, *J. Phys. Chem. C*, 2017, **121**, 13448–13456.
- 17 T. Hosokai, H. Matsuzaki, H. Nakanotani, K. Tokumaru, T. Tsutsui, A. Furube, K. Nasu, H. Nomura, M. Yahiro and C. Adachi, *Sci. Adv.*, 2017, **3**, e1603282.
- 18 K. R. Naveen, P. Palanisamy, M. Y. Chae and J. H. Kwon, *Chem. Commun.*, 2023, **59**, 3685–3702.
- 19 Q. Zhang, H. Kuwabara, W. J. Potscavage, S. Huang, Y. Hatae, T. Shibata and C. Adachi, *J. Am. Chem. Soc.*, 2014, **136**, 18070–18081.
- 20 Z. Kuang, G. He, H. Song, X. Wang, Z. Hu, H. Sun, Y. Wan, Q. Guo and A. Xia, *J. Phys. Chem. C*, 2018, **122**, 3727–3737.
- 21 J. A. Treadway, B. Loeb, R. Lopez, P. A. Anderson, F. R. Keene and T. J. Meyer, *Inorg. Chem.*, 1996, **35**, 2242–2246.
- 22 T. Ogiwara, Y. Wakikawa and T. Ikoma, *J. Phys. Chem. A*, 2015, **119**, 3415–3418.
- 23 R. Englman and J. Jortner, *Mol. Phys.*, 1970, **18**, 145–164.
- 24 Y.-C. Wei, S. F. Wang, Y. Hu, L.-S. Liao, D.-G. Chen, K.-H. Chang, C.-W. Wang, S.-H. Liu, W.-H. Chan, J.-L. Liao, W.-Y. Hung, T.-H. Wang, P.-T. Chen, H.-F. Hsu, Y. Chi and P.-T. Chou, *Nat. Photonics*, 2020, **14**, 570–577.
- 25 C. E. Whittle, J. A. Weinstein, M. W. George and K. S. Schanze, *Inorg. Chem.*, 2001, **40**, 4053–4062.
- 26 J. S. Wilson, N. Chawdhury, M. R. A. Al-Mandhary, M. Younus, M. S. Khan, P. R. Raithby, A. Köhler and R. H. Friend, *J. Am. Chem. Soc.*, 2001, **123**, 9412–9417.
- 27 J. V. Caspar and T. J. Meyer, *J. Phys. Chem.*, 1983, **87**, 952–957.
- 28 Y. Xiao, H. Wang, Z. Xie, M. Shen, R. Huang, Y. Miao, G. Liu, T. Yu and W. Huang, *Chem. Sci.*, 2022, **13**, 8906–8923.
- 29 Y. Liu, X. Xiao, Y. Ran, Z. Bin and J. You, *Chem. Sci.*, 2021, **12**, 9408–9412.
- 30 C. Wang, X. Li, Y. Gao, L. Wang, S. Zhang, L. Zhao, P. Lu, B. Yang, S. Su and Y. Ma, *Adv. Opt. Mater.*, 2017, **5**, 1700441.
- 31 A. Abdurahman, Y. Chen, X. Ai, O. Ablikim, Y. Gao, S. Dong, B. Li, B. Yang, M. Zhang and F. Li, *J. Mater. Chem. C*, 2018, **6**, 11248–11254.



- 32 T.-L. Wu, M.-J. Huang, C.-C. Lin, P.-Y. Huang, T.-Y. Chou, R.-W. Chen-Cheng, H.-W. Lin, R.-S. Liu and C.-H. Cheng, *Nat. Photonics*, 2018, **12**, 235–240.
- 33 H. J. Kim, H. Kang, J. Jeong, S. H. Park, C. W. Koh, C. W. Kim, H. Y. Woo, M. J. Cho, S. Park and D. H. Choi, *Adv. Funct. Mater.*, 2021, **31**, 2102588.
- 34 X. Tang, Q. Bai, T. Shan, J. Li, Y. Gao, F. Liu, H. Liu, Q. Peng, B. Yang, F. Li and P. Lu, *Adv. Funct. Mater.*, 2018, **28**, 1705813.
- 35 S. Sharma and A. K. Pal, *J. Mater. Chem. C*, 2022, **10**, 15681–15707.
- 36 G. Chen, J. R. Swartzfager and J. B. Asbury, *J. Am. Chem. Soc.*, 2023, **145**, 25495–25504.
- 37 Y. Liu, J. Yang, Z. Mao, Y. Wang, J. Zhao, S.-J. Su and Z. Chi, *Chem. Sci.*, 2023, **14**, 1551–1556.
- 38 Y. Liu, C. Li, Z. Ren, S. Yan and M. R. Bryce, *Nat. Rev. Mater.*, 2018, **3**, 18020.
- 39 J. Xu, Y. Dai, J. Zhang, Z. Jia, Q. Meng and J. Qiao, *Adv. Opt. Mater.*, 2023, 2300989.
- 40 Z. Li, J.-R. Zhang, X.-K. Tian, S. Yang, S. Chen, H. Zhou and X.-G. Yang, *Chem. Sci.*, 2022, **13**, 9381–9386.
- 41 W. Zhang, H. Song, J. Kong, Z. Kuang, M. Li, Q. Guo, C. Chen and A. Xia, *J. Phys. Chem. C*, 2019, **123**, 19322–19332.
- 42 H. Miranda-Salinas, A. Rodriguez-Serrano, J. M. Kaminski, F. Dinkelbach, N. Hiromichi, Y. Kusakabe, H. Kaji, C. M. Marian and A. P. Monkman, *J. Phys. Chem. C*, 2023, **127**, 8607–8617.
- 43 T. Yang, B. Liang, Z. Cheng, C. Li, G. Lu and Y. Wang, *J. Phys. Chem. C*, 2019, **123**, 18585–18592.
- 44 J.-L. He, Y. Tang, K. Zhang, Y. Zhao, Y.-C. Lin, C.-K. Hsu, C.-H. Chen, T.-L. Chiu, J.-H. Lee, C.-K. Wang, C.-C. Wu and J. Fan, *Mater. Horiz.*, 2022, **9**, 772–779.
- 45 D. Karthik, Y. H. Jung, H. Lee, S. Hwang, B. Seo, J. Kim, C. W. Han and J. H. Kwon, *Adv. Mater.*, 2021, **33**, 2007724.
- 46 D. H. Ahn, S. W. Kim, H. Lee, I. J. Ko, D. Karthik, J. Y. Lee and J. H. Kwon, *Nat. Photonics*, 2019, **13**, 540–546.
- 47 P. J. B. Claricoats, *Proc. IEE-Part C Monogr.*, 1962, **109**, 401.
- 48 Z. Tang, C. Chang, F. Bao, L. Tian, H. Liu, M. Wang, C. Zhu and J. Xu, *Polymers*, 2021, **13**, 284.
- 49 X. Niu, P. Gautam, Z. Kuang, C. P. Yu, Y. Guo, H. Song, Q. Guo, J. M. W. Chan and A. Xia, *Phys. Chem. Chem. Phys.*, 2019, **21**, 17323–17331.
- 50 W. Zhang, J. Kong, D. Hu, M. Tao, X. Niu, S. Vdović, D. Aumiller, Y. Ma and A. Xia, *J. Phys. Chem. C*, 2020, **124**, 5574–5582.
- 51 M. K. Etherington, J. Gibson, H. F. Higginbotham, T. J. Penfold and A. P. Monkman, *Nat. Commun.*, 2016, **7**, 13680.
- 52 J. Gibson, A. P. Monkman and T. J. Penfold, *ChemPhysChem*, 2016, **17**, 2956–2961.
- 53 Y. Wang, Z. Guo, Y. Gao, Y. Tian, Y. Deng, X. Ma and W. Yang, *J. Phys. Chem. Lett.*, 2022, **13**, 6664–6673.
- 54 Y. Wang, Y. Tian, Y. Gao, Z. Guo, Z. Xue, Y. Han, W. Yang and X. Ma, *J. Phys. Chem. Lett.*, 2023, **14**, 9665–9676.
- 55 H. Sun, C. Zhong and J.-L. Brédas, *J. Chem. Theory Comput.*, 2015, **11**, 3851–3858.
- 56 X. Zhao and J. Zhao, *Chem. Commun.*, 2022, **58**, 7666–7669.
- 57 H. Noda, H. Nakanotani and C. Adachi, *Chem. Lett.*, 2019, **48**, 126–129.
- 58 Q. Ou, Y. Shao and Z. Shuai, *J. Am. Chem. Soc.*, 2021, **143**, 17786–17792.
- 59 N. Aizawa, Y. Harabuchi, S. Maeda and Y.-J. Pu, *Nat. Commun.*, 2020, **11**, 3909.
- 60 Y. Olivier, B. Yurash, L. Muccioli, G. D'Avino, O. Mikhnenko, J. C. Sancho-García, C. Adachi, T.-Q. Nguyen and D. Beljonne, *Phys. Rev. Mater.*, 2017, **1**, 075602.
- 61 S. Lin, Z. Pei, B. Zhang, H. Ma and W. Liang, *J. Phys. Chem. A*, 2022, **126**, 239–248.
- 62 J. Tatchen, N. Gilka and C. M. Marian, *Phys. Chem. Chem. Phys.*, 2007, **9**, 5209.
- 63 B. R. Henry and W. Siebrand, *J. Chem. Phys.*, 1971, **54**, 1072–1085.
- 64 K. A. Zachariasse, M. Grobys, I. Riickert and W. Kiihnle, *J. Photochem. Photobiol., A*, 1997, **105**, 373–383.
- 65 M. C. Drummer, R. B. Weerasooriya, N. Gupta, B. T. Phelan, A. J. S. Valentine, A. A. Cordones, X. Li, L. X. Chen and K. D. Glusac, *J. Phys. Chem. C*, 2022, **126**, 1946–1957.
- 66 T. Bolze, J. Wree, F. Kanal, D. Schleier and P. Nuernberger, *ChemPhysChem*, 2018, **19**, 138–147.
- 67 H. Song, H. Zhao, Y. Guo, A. M. Philip, Q. Guo, M. Hariharan and A. Xia, *J. Phys. Chem. C*, 2020, **124**, 237–245.
- 68 J. Köhler, T. Quast, J. Buback, I. Fischer, T. Brixner, P. Nuernberger, B. Geiß, J. Mager and C. Lambert, *Phys. Chem. Chem. Phys.*, 2012, **14**, 11081.
- 69 Y. Rout, C. Montanari, E. Pasciucco, R. Misra and B. Carloti, *J. Am. Chem. Soc.*, 2021, **143**, 9933–9943.
- 70 Z. Zhang, Y.-S. Wu, K.-C. Tang, C.-L. Chen, J.-W. Ho, J. Su, H. Tian and P.-T. Chou, *J. Am. Chem. Soc.*, 2015, **137**, 8509–8520.
- 71 Y. Chen, K.-H. Chang, F.-Y. Meng, S.-M. Tseng and P.-T. Chou, *Angew. Chem., Int. Ed.*, 2021, **60**, 7205–7212.
- 72 Z. Ma, Z. Yang, L. Mu, L. Deng, L. Chen, B. Wang, X. Qiao, D. Hu, B. Yang, D. Ma, J. Peng and Y. Ma, *Chem. Sci.*, 2021, **12**, 14808–14814.
- 73 Y. Wen, S. Xiao, H. Liu, X. Tian, J. De, T. Lu, Z. Yang, D. Zou, Y. Lv, S.-T. Zhang, Q. Su and B. Yang, *J. Mater. Chem. C*, 2021, **9**, 17511–17517.
- 74 V. Karunakaran and S. Das, *J. Phys. Chem. B*, 2016, **120**, 7016–7023.
- 75 Y. Gao, Y. Wang, Z. Guo, Y. Wan, C. Li, B. Yang, W. Yang and X. Ma, *J. Phys. Chem. B*, 2022, **126**, 2729–2739.
- 76 C.-W. Ju, B. Li, L. Li, W. Yan, C. Cui, X. Ma and D. Zhao, *J. Am. Chem. Soc.*, 2021, **143**, 5903–5916.
- 77 H. Gao, S. Shen, Y. Qin, G. Liu, T. Gao, X. Dong, Z. Pang, X. Xie, P. Wang and Y. Wang, *J. Phys. Chem. Lett.*, 2022, 7561–7567.
- 78 J. Bahrenburg, F. Renth, F. Temps, F. Plamper and W. Richtering, *Phys. Chem. Chem. Phys.*, 2014, **16**, 11549.
- 79 H.-M. Pan, C.-C. Wu, C.-Y. Lin, C.-S. Hsu, Y.-C. Tsai, P. Chowdhury, C.-H. Wang, K.-H. Chang, C.-H. Yang, M.-H. Liu, Y.-C. Chen, S.-P. Su, Y.-J. Lee, H. K. Chiang, Y.-H. Chan and P.-T. Chou, *J. Am. Chem. Soc.*, 2023, **145**, 516–526.



- 80 Y.-C. Wei, B.-H. Chen, R.-S. Ye, H.-W. Huang, J.-X. Su, C.-Y. Lin, J. Hodgkiss, L.-Y. Hsu, Y. Chi, K. Chen, C.-H. Lu, S.-D. Yang and P.-T. Chou, *Angew. Chem., Int. Ed.*, 2023, **62**, e202300815.
- 81 C. Fanggao, G. A. Saunders, E. F. Lambson, R. N. Hampton, G. Carini, G. Di Marco and M. Lanza, *J. Polym. Sci., Part B: Polym. Phys.*, 1996, **34**, 425–433.
- 82 M. Hénot, A. Chennevière, E. Drockenmuller, K. Shull, L. Léger and F. Restagno, *Eur. Phys. J. E*, 2017, **40**, 11.

